

RESEARCH ARTICLE | MAY 19 2023

Effect of porous coatings on the nonlinear evolution of Mack modes in hypersonic boundary layers

Song Qinyang (宋沁杨) ; Zhao Lei (赵磊)  ; Dong Ming (董明)  

 Check for updates

Physics of Fluids 35, 054115 (2023)

<https://doi.org/10.1063/5.0148065>



Biomechanics
Special Topic:
Microfluidic Biosensors

Submit Today

Effect of porous coatings on the nonlinear evolution of Mack modes in hypersonic boundary layers

Cite as: Phys. Fluids **35**, 054115 (2023); doi: 10.1063/5.0148065

Submitted: 28 February 2023 · Accepted: 5 May 2023 ·

Published Online: 19 May 2023



View Online



Export Citation



CrossMark

Qinyang Song (宋沁杨),^{1,2}  Lei Zhao (赵磊),^{2,3,a)}  and Ming Dong (董明)^{1,a)} 

AFFILIATIONS

¹State Key Laboratory of Nonlinear Mechanics, Institute of Mechanics, Chinese Academy of Sciences, Beijing 100190, China

²Department of Mechanics, School of Mechanical Engineering, Tianjin University, Tianjin 300350, China

³Tianjin Key Laboratory of Modern Engineering Mechanics, Tianjin 300350, China

^{a)} Authors to whom correspondence should be addressed: lei_zhao@tju.edu.cn and dongming@imech.ac.cn

ABSTRACT

The influence of a porous wall on the nonlinear evolution of Mack modes in a hypersonic boundary layer is studied by solving the nonlinear parabolized stability equations. The fundamental resonance of the second mode is particularly considered. It is found that the porous effect leads to (1) a much stronger mean-flow distortion in an indirect way, (2) a greater suppression of the saturated fundamental mode, and (3) slower amplification rates of the secondary instability modes, which eventually delays the transition onset. Detailed explanations of the three mechanisms are provided.

Published under an exclusive license by AIP Publishing. <https://doi.org/10.1063/5.0148065>

I. INTRODUCTION

Laminar-flow control (LFC) to postpone the laminar-turbulent transition is a desired strategy in the aerodynamic design for high-speed flying vehicles, because the drag and heat flux in the laminar phase are smaller than those in the turbulent phase. At flight conditions, the level of the environmental perturbations is usually low, and the laminar-turbulent transition follows a natural route, for which the receptivity, linear instability, nonlinear breakdown, and turbulence appear in sequence.¹ For a quasi-two-dimensional hypersonic boundary layer, the most unstable mode is the Mack second mode,² which, in the high-Reynolds-number asymptotic framework, shows a double-deck structure, an inviscid region in the bulk of the boundary layer and a viscous Stokes layer in the vicinity of the wall.^{3,4} The pressure perturbation of the inviscid mode oscillates in the bulk region of the boundary layer and impinges on and reflects by the wall, so that the mode behaves as an acoustic wave being reflected between the wall and the sonic line.⁵ Thus, if the property of the wall is altered such that the reflected acoustic wave changes its phase to cancel out partially the incident acoustic wave, then the growth of the Mack second mode could be suppressed. Such an idea is realized by replacing the smooth wall by a porous coating.⁵

Using a semi-transparent wall as a simplified model, Malmuth *et al.*⁶ studied the linear instability of the Mack modes, and the substantial stabilizing effect on the second mode was observed. A more

practical model for a porous wall consisting of equally spaced micro-holes was studied by Fedorov *et al.*,⁷ for which the perturbation transverse velocity at the wall \hat{v}_w is related linearly to the perturbation transverse pressure \hat{p}_w , with a complex admittance coefficient A_y , i.e., $\hat{v}_w = A_y \hat{p}_w$, where A_y is dependent on the porous-wall property and the instability frequency. The results also suggested a strong stabilizing effect of the porous coating on the majority of the second mode, but a weak destabilizing effect on the first mode and the low-frequency band of the second mode. More profound stabilization of the second mode was observed for cold walls. These phenomena were subsequently confirmed by quite a few theoretical,^{8–10} numerical,^{11,12} and experimental^{13–15} works. Additionally, if the surface is partially covered by porous coatings, then the junction of the smooth and porous walls may lead to a scattering effect due to the sudden change of the wall boundary condition of the perturbation, which was studied systematically by Song and Zhao¹⁶ based on the harmonic linearized Navier-Stokes equations (HLNS).

The aforementioned studies only focus on the linear evolution of Mack modes over porous coatings. Actually, in the widely used e- N transition prediction method, the choice of the N factor, representing the amplitude accumulation, relies on both the receptivity and the nonlinear processes. The receptivity process determines the initial amplitudes of the Mack modes, and for a rigid-wall configuration, the

local receptivity mechanisms of the inviscid and viscous Mack modes were studied theoretically by Refs. 3 and 17, respectively. As pointed out by Song and Zhao,¹⁶ it is favorable to introduce a porous panel in a downstream location, and so the study of the rigid-wall configuration is sufficient. The nonlinear process determines the transition threshold, which may be different for different nonlinear interaction regimes.¹⁸ For example, the perturbations for the fundamental resonance,¹⁹ appearing among a dominant planar mode and a pair of small oblique modes with the same frequency, develop in a much longer streamwise region than that for the oblique breakdown regime. Therefore, the equivalent transition thresholds for the two regimes should be different. Experimental and numerical studies^{20–22} reported that for the fundamental resonance, which is usually an efficient mechanism to trigger transition in hypersonic boundary layers, the application of the porous wall would stabilize the perturbations in the nonlinear phase, leading to a significant delay of transition. This phenomenon was attributed to the disruption of the phase-locked regime by the porous wall, which prevents the growth of the secondary instability.²² However, such an explanation was obtained only by observing the growth rates, phase speeds, and perturbation profiles of the Fourier modes, and the dynamic mechanism leading to the disruption of the phase-locked regime is not well understood. Actually, the porous walls can change the amplitude amplification of each unsteady Fourier mode through an admittance boundary condition, which is dependent on its frequency, and the mean-flow distortion (MFD) induced by the Reynolds stress could be indirectly affected, the change of which determines the movement of the transition onset. An in-depth analysis is required to build the link between the porous effect and the nonlinear transition, which is to be performed in this paper.

II. MATHEMATICAL DESCRIPTION

A. Physical model and governing equations

As sketched in Fig. 1, we consider a hypersonic boundary-layer flow over a thin and isothermal flat plate. The oncoming flow is assumed to be a perfect gas. A weak oblique shock wave forms from the sharp leading edge of the plate. Most of the plate surface is coated by a porous media made of fibrous absorbent material, as shown by the blue region in Fig. 1, whose impact on the unsteady perturbations can be formulated by an admittance boundary condition.^{8,10} For a selected computational domain, we introduce a set of Mack instability modes as inflow perturbations and calculate their evolution until the nonlinear phase.

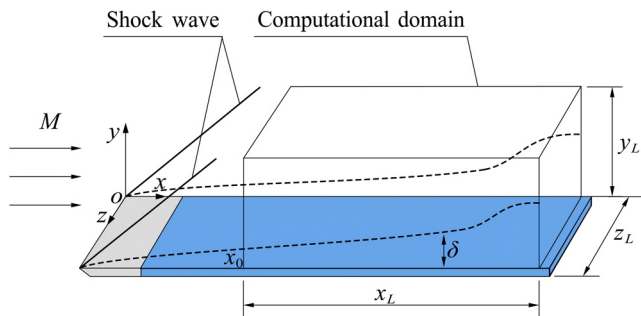


FIG. 1. Sketch of the physical model, where the blue region at the wall denotes the porous-coating panel.

The three-dimensional (3D) Cartesian coordinate system (x^*, y^*, z^*) is employed in this paper, with its origin located at the leading edge of the plate. We introduce a reference length L_{ref}^* and take the oncoming-flow velocity U_∞^* as the reference velocity. The coordinate system (x, y, z) and time t are normalized as

$$(x, y, z) = (x^*, y^*, z^*)/L_{ref}^*, \quad t = t^*U_\infty^*/L_{ref}^*. \quad (1)$$

The instantaneous density ρ , velocity field $\mathbf{u} = (u, v, w)$, temperature T , and pressure p are normalized as

$$(\rho, \mathbf{u}, T, p) = (\rho^*/\rho_\infty^*, \mathbf{u}^*/U_\infty^*, T^*/T_\infty^*, p^*/(\rho_\infty^*U_\infty^{*2})), \quad (2)$$

where ρ_∞^* and T_∞^* are the oncoming density and temperature, respectively. The oncoming Mach number and Reynolds number are defined as $M = U_\infty^*/a_\infty^*$ and $R = \rho_\infty^*U_\infty^*L_{ref}^*/\mu_\infty^*$, where a_∞^* and μ_∞^* denote the dimensional sound speed and dynamic viscosity of the oncoming flow, respectively. The subscript ∞ and superscript asterisk represent the oncoming flow and dimensional quantities, respectively.

The dimensionless compressible Navier–Stokes equations governing the flow motion are

$$\begin{aligned} \frac{\partial \rho}{\partial t} + \nabla \cdot (\rho \mathbf{u}) &= 0, \\ \rho \frac{D\mathbf{u}}{Dt} &= -\nabla p + \frac{1}{R} \left[2\nabla \cdot (\mu \mathbf{S}) - \frac{2}{3} \nabla (\mu \nabla \cdot \mathbf{u}) \right], \\ \rho \frac{DT}{Dt} &= (\gamma - 1)M^2 \left[\frac{Dp}{Dt} + \frac{2\mu \mathbf{S} : \mathbf{S} - \frac{2}{3} \mu (\nabla \cdot \mathbf{u})^2}{R} \right] \\ &\quad + \frac{\nabla \cdot (\mu \nabla T)}{RPr}, \\ \gamma M^2 p &= \rho T, \end{aligned} \quad (3)$$

where $\gamma = 1.4$ is the ratio of the specific heats, $Pr = 0.72$ is the Prandtl number, $\mathbf{S} = [\nabla \mathbf{u} + (\nabla \mathbf{u})^T]/2$ is the strain rate tensor, and ‘:’ represents the double-dot product of two second-order tensors. The dimensionless dynamic viscosity μ is approximated by the Sutherland’s law, i.e., $\mu(T) = (1 + T_\mu)T^{3/2}/(T + T_\mu)$ with $T_\mu = 110.4 \text{ K}/T_\infty^*$. The instantaneous flow $\phi \equiv (\rho, \mathbf{u}, T, p)$ can be decomposed into a steady base flow $\Phi_B \equiv (\rho_B, \mathbf{U}_B, T_B, p_B)$ and an unsteady perturbation $\phi' \equiv (\rho', \mathbf{u}', T', p')$, namely,

$$\phi(x, y, z, t) = \Phi_B(x, y) + \phi'(x, y, z, t). \quad (4)$$

B. Two-dimensional (2D) base flow

Since the streamwise and spanwise length scales of the porous coating are much smaller than the boundary-layer thickness, the porous wall has little impact on the base flow. For a selected 2D computational domain $[x_0, x_0 + x_L] \times [0, y_L]$, we use the Navier–Stokes solver to calculate the base flow by introducing the compressible Blasius solution as the inflow perturbation. Our in-house Navier–Stokes solver was also used in a few previous works.^{4,23–26} The wall conditions are

$$U_B = V_B = W_B = 0, \quad T_B = T_w \quad \text{at } y = 0, \quad (5)$$

where T_w is the dimensionless wall temperature. The outflow condition is employed at the upper boundary, and a buffer zone is employed at the outlet boundary.

C. Perturbations

1. Admittance condition for the perturbation at a porous surface

Following Fedorov *et al.*,^{8,10} the admittance of the porous coating is given by

$$A_y(\omega) = -\frac{n}{Z_0} \tanh(\Lambda h), \tag{6}$$

where n denotes the porosity, and $h = h^*/L_{ref}^*$ represents the dimensionless porous-layer thickness. The characteristic impedance Z_0 and propagation constant Λ are calculated based on the analytical solution in Johnson *et al.*,²⁷

$$Z_0 = \frac{\sqrt{\tilde{\rho}/\tilde{C}}}{M\sqrt{T_w}}, \quad \Lambda = -\frac{i\omega M}{\sqrt{T_w}} \sqrt{\tilde{\rho}\tilde{C}}, \tag{7}$$

where

$$\tilde{\rho} = \alpha_\infty \left[1 + \frac{g(\lambda_1)}{\lambda_1} \right], \quad \tilde{C} = \gamma - \frac{\gamma - 1}{1 + g(\lambda_2)/\lambda_2}, \tag{8}$$

$$g(\lambda) = \sqrt{1 + \frac{4\alpha_\infty \mu_w^* \lambda}{\sigma^* n r_p^{*2}}}, \quad \lambda_1 = \frac{-i\alpha_\infty \rho_w^* \omega^*}{n\sigma^*}, \quad \lambda_2 = 4Pr\lambda_1,$$

where ω and ω^* are the dimensionless and dimensional instability frequencies. μ_w^* and ρ_w^* are the dimensional viscosity and density at the wall. σ^* is the flow resistivity, and α_∞ is the tortuosity of the porous layer. The characteristic pore size r_p^* is related to the fiber diameter d^* through the porosity n ,

$$r_p^* = \frac{\pi d^{*2}}{2(1-n)(2-n)}. \tag{9}$$

2. Linear stability theory (LST)

The evolution of an infinitesimal perturbation can be approximately predicted by the LST under the parallel-flow assumption. We express the perturbation field $\phi' \equiv (\rho', \mathbf{u}', T', p')$ as a travelling-wave form,

$$\phi'(x, y, z, t) = \varepsilon \hat{\phi}(y) e^{i(\alpha x + \beta z - \omega t)} + \text{c.c.}, \tag{10}$$

where $i = \sqrt{-1}$, ω is the perturbation frequency, α is the streamwise wavenumber, and β is the spanwise wavenumber. $\hat{\phi} \equiv (\hat{\rho}, \hat{\mathbf{u}}, \hat{T}, \hat{p})$ is the shape function, $\varepsilon \ll 1$ is the amplitude, and c.c. is the complex conjugate. For a spatial mode, the frequency ω and the spanwise wavenumber β are given to be real, and $\alpha = \alpha_r + i\alpha_i$ is complex with $-\alpha_i$ denoting its streamwise growth rate. Substituting Eq. (10) in the Navier–Stokes equations and neglecting the non-parallelism of the base flow and the $O(\varepsilon^2)$ terms, we obtain the compressible Orr–Sommerfeld (O-S) equations,

$$L_{OS} \left(\hat{u}, \frac{d\hat{u}}{dy}, \hat{v}, \hat{p}, \hat{T}, \frac{d\hat{T}}{dy}, \hat{w}, \frac{d\hat{w}}{dy} \right)^\top = 0, \tag{11}$$

where the O-S operator L_{OS} is a function of Φ_B and can be found in Refs. 28 and 29. Unless the wall temperature is extremely cold, for

which a radiation mode with an oscillatory far-field boundary condition appears around the upper-branch neutral frequency (see Refs. 25 and 30), most of the instability modes are attenuated in the far field, leading to the boundary conditions,

$$\hat{u} = \hat{v} = \hat{w} = \hat{T} \rightarrow 0 \quad \text{as } y \rightarrow \infty. \tag{12}$$

For a porous wall, the no-slip, isothermal, and admittance boundary conditions are employed at the wall,

$$\hat{u} = \hat{w} = \hat{T} = 0, \quad \hat{v} = A_y(\omega) \hat{p} \quad \text{at } y = 0. \tag{13}$$

However, for a smooth wall, the boundary condition in Eq. (13) should be replaced by the non-penetration condition,

$$\hat{u} = \hat{v} = \hat{w} = \hat{T} = 0 \quad \text{at } y = 0. \tag{14}$$

The O-S equations [Eq. (11)] with the homogeneous boundary conditions [Eqs. (12) and (13) or Eq. (14)] form an eigenvalue problem, which can be solved following the numerical approach in Ref. 28.

3. Parabolized stability equation (PSE)

When the perturbations acquire, through accumulated linear growth, finite amplitudes, the nonlinearity needs to be taken into account, and so the LST prediction ceases to be valid. Thus, the PSE approach,^{31–36} which takes both the non-parallelism and nonlinearity into account, is employed. Now, the perturbation ϕ' is expressed in terms of a truncated Fourier series,

$$\phi'(x, y, z, t) = \sum_{m=-M}^M \sum_{n=-N}^N \varepsilon_{m,n} \tilde{\phi}_{m,n}(x, y) e^{i \left[\int_{x_0}^x \alpha_{m,n}(\bar{x}) d\bar{x} + n\beta_0 z - m\omega_0 t \right]}, \tag{15}$$

where ω_0 and β_0 are the fundamental frequency and spanwise wavenumber, respectively, m and n denote the orders of ω and β , respectively, $\varepsilon_{m,n}$, $\tilde{\phi}_{m,n} \equiv (\tilde{\rho}_{m,n}, \tilde{\mathbf{u}}_{m,n}, \tilde{T}_{m,n})$, and $\alpha_{m,n}$ represent the amplitude, shape function, and complex wavenumber of the harmonic mode, respectively, and M and N denote the limiting order of the truncation for the frequency and spanwise wavenumber, respectively. The shape function $\tilde{\phi}_{m,n}$ varies slowly with x .

Substituting Eq. (15) in the compressible Navier–Stokes equations [Eq. (3)], subtracting out the terms governing the base flow, and neglecting the terms with ∂_{xx} and ∂_{xy} , we obtain the parabolized stability equations,

$$\left(\tilde{\mathbf{A}}_{m,n} \frac{\partial}{\partial x} + \tilde{\mathbf{B}}_{m,n} \frac{\partial}{\partial y} + \tilde{\mathbf{D}}_{m,n} + \mathbf{V}_{yy} \frac{\partial^2}{\partial y^2} \right) \tilde{\phi}_{m,n} = \tilde{\mathbf{F}}_{m,n} e^{-i \int_{x_0}^x \alpha_{m,n}(\bar{x}) d\bar{x}}, \tag{16}$$

where the coefficient matrices $\tilde{\mathbf{A}}_{m,n}$, $\tilde{\mathbf{B}}_{m,n}$, $\tilde{\mathbf{D}}_{m,n}$, \mathbf{V}_{yy} and the nonlinear term $\tilde{\mathbf{F}}_{m,n}$ can be found in Refs. 34 and 36. Since the ∂_{xx} terms are neglected, the elliptic N-S equations are parabolized, leading to a significant simplification of the system. We neglect the ∂_{xy} terms here only for simplicity because they are numerically small.

If the terms on the right-hand side of Eq. (16) is set to be zero, then the system is linearized, which is referred to as the linear parabolized stability equation (LPSE). To be distinguished, the approach by taking into account a non-zero $\tilde{\mathbf{F}}_{m,n}$ is referred to as the nonlinear

parabolized stability equation (NPSE). In the nonlinear phase, the amplitudes of \tilde{u} and \tilde{T} reach $O(0.01)$, but the perturbation pressure \tilde{p} and the perturbation transverse velocity \tilde{v} in the near-wall region are still small, and so the admittance boundary condition [Eq. (13)] is still valid for each individual Fourier component.

4. Direct numerical simulation (DNS) with the admittance condition

To confirm the accuracy of the PSE calculations, the DNS approach for the porous-wall configuration is employed. For a smooth-wall configuration, the DNS approach is the same as our previous works.^{4,23–26} However, for porous walls, the wall boundary condition needs to be modified. For the linear evolution of the Mack mode over a porous wall, Song and Zhao¹⁶ developed a numerical treatment to consider the admittance boundary condition, which, however, does not apply if perturbations with more than one frequency are considered. The latter is of our concern in this paper, and an improved treatment is developed in the following.

We express the wall perturbations of the pressure p' and the transverse velocity v' in terms of a Fourier series,

$$(p', v')(x, 0, z, t) = \sum_{m=-M}^M (\tilde{p}_m, \tilde{v}_m)(x, z)e^{-im\omega_0 t}, \quad (17)$$

where \tilde{p}_m and \tilde{v}_m denote the shape functions of the Fourier mode for $\omega = m\omega_0$. According to Eq. (13), we know that

$$\tilde{v}_m(x, z) = A_y(m\omega_0)\tilde{p}_m(x, z). \quad (18)$$

For a zero frequency, we have $A_y(0) = 0$. Then, the transverse velocity perturbation in the physical space is expressed as

$$v'(x, 0, z, t) = \sum_{m=-M}^M A_y(m\omega_0)\tilde{p}_m(x, z)e^{-im\omega_0 t}. \quad (19)$$

In the numerical process, we can calculate $\tilde{p}_m(x, z)$ at any time $t_0 > T_p$ using the data $p'(x, 0, z, t)$ from $t = t_0 - T_p$ to $t = t_0$,

$$\tilde{p}_m(x, z) = \frac{\omega_0}{2\pi} \int_{t_0 - T_p}^{t_0} p'(x, 0, z, t)e^{im\omega_0 t} dt, \quad (20)$$

where $T_p = 2\pi/\omega_0$ represents the time period based on the frequency of the fundamental mode.

III. RESULTS AND DISCUSSION

A. Flow parameters

The flow parameters are presented in Table I, and they are the representative experimental configuration³⁷ and have been used for many numerical studies.^{16,23,38} The wall temperature T_w is almost the same as the adiabatic temperature of the Blasius solution, and thus, the heat flux at the wall in the early laminar phase is almost zero.

TABLE I. Parameters of the oncoming stream.

M	R	T_∞^* (K)	T_w	ρ_∞^* (kg/m ³)	L_{ref}^* (m)
5.92	13200	48.69	6.88	5.32×10^{-2}	1.00×10^{-3}

TABLE II. Parameters of the porous wall.

α_∞	σ^* [kg/(m ³ s)]	n	d^* (m)	h^* (m)
1.00	1.66×10^5	0.75	3.00×10^{-5}	7.50×10^{-4}

The parameters of the porous-wall property introduced in Eqs. (7) and (8) are listed in Table II, which are the same as those in Refs. 8 and 16.

In this paper, we also perform calculations for a smooth-wall configuration for comparison, and the porous-wall and smooth-wall cases are referred to as case P and case S, respectively. In the calculation of the base flow, we set $x_0 = 300$, $x_L = 400$, and $y_L = 100$. We use 2001 uniform grid points in the streamwise direction, and 151 nonuniform grid points that are clustered near the wall are employed in the wall-normal direction. An additional sponge region is introduced for $x \in [700, 900]$, with 100 nonuniform grid points allocated. Such a mesh system was also employed in our previous study.¹⁶ In the PSE calculations, the same computational domain and wall-normal mesh system are employed, and the number of the grid points in the streamwise direction is reduced to 201. A careful resolution test has performed to confirm the accuracy of the PSE calculations.

B. Base flow and linear instability characteristics

The base-flow profiles of the streamwise velocity U_B and temperature T_B at $x = 300$ are shown in Fig. 2, where the nominal boundary-layer thickness $\delta_{99} \approx 3.04$ is marked in panel (a). Based on this base flow, the contours of the growth rates in the $\beta - \omega$ plane for the porous (right) and smooth (left) walls are compared in Fig. 3(a). Two unstable regions are observed for each case: (1) The first mode appears in the low-frequency band, for which the most unstable mode is a 3D oblique wave, and (2) the second mode appears in the high-frequency band, for which the most unstable mode is a 2D planar wave. The second mode is more unstable than the first mode. In most of the second-mode frequency band, the growth rate for case P is considerably smaller than that for case S, indicating a significant stabilizing

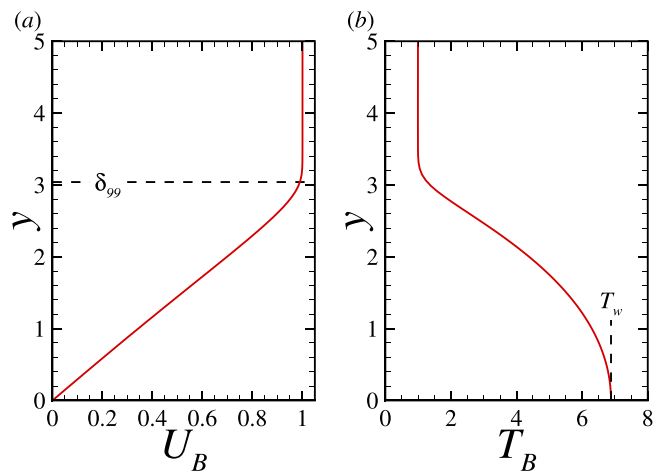


FIG. 2. Base-flow profiles of the streamwise velocity U_B (a) and temperature T_B (b) at $x = 300$.

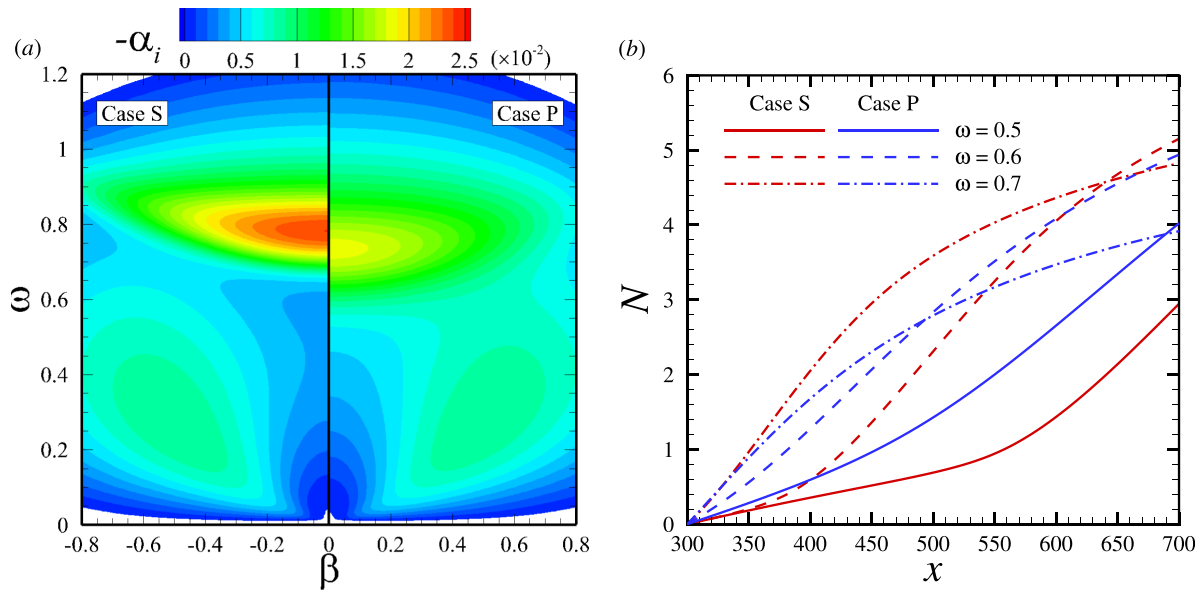


FIG. 3. (a) Comparison of the contours of $-\alpha_i$ in the $\beta - \omega$ plane between cases S and P at $x = 300$ and (b) N -factor evolution of the 2D Mack modes for different frequencies predicted by LST.

effect of the porous wall. However, when the frequency is relatively low (lower than around 0.7), the porous wall plays a weak destabilizing effect. The eigenfunctions of $(|\hat{u}|, |\hat{v}|, |\hat{\rho}|, |\hat{T}|)$ for cases S and P are compared in Fig. 4, which are normalized by the maximum of $|\hat{u}|$ for each case. The shapes of each quantity for the two cases are quite close, and the only difference is that the transverse velocity perturbation $|\hat{v}|$ is slightly greater in the near-wall region for case P, due to the presence of the admittance boundary condition.

Since the boundary-layer thickness grows with x , the instability property changes as the perturbation propagates downstream. The accumulated amplitude of a linear perturbation can be predicted by the N factor, defined by $N(x) = \int_{x_0}^x -\alpha_i(\bar{x})d\bar{x}$. Choosing three representative frequencies, Fig. 3(b) compares the N -factor evolution of the planar Mack modes for cases S and P. For a high frequency, $\omega = 0.7$, the N value for case P is lower than that for case S, while the opposite

is true for a low frequency ($\omega = 0.5$). The fundamental frequency of the following calculations for the fundamental resonance is selected to be $\omega = 0.6$, for which the linearly accumulated amplitudes for cases S and P are similar in the whole domain.

C. Nonlinear evolution of the Mack modes

1. Calculations for the fundamental resonance

The initial perturbations for the NPSE calculation consist of a high-amplitude ($\varepsilon_{1,0} = 0.005$) 2D second mode with $\omega_0 = 0.6$ (denoted by the fundamental mode) and a pair of low-amplitude ($\varepsilon_{1,\pm 1} = 1 \times 10^{-5}$) oblique second mode with the same frequency but the opposite spanwise wavenumber ($\pm \beta_0$ with $\beta_0 = 0.4$). For convenience, we denote a Fourier mode with a frequency $m\omega_0$ and a spanwise wavenumber $n\beta_0$ by (m, n) , and thus, the introduced 2D and 3D perturbations are denoted by $(1,0)$ and $(1,\pm 1)$, respectively. In the nonlinear phase, the low-amplitude oblique waves gain energy from the finite-amplitude 2D mode and are amplified by a much greater growth rate. Meanwhile, the high-order harmonics $(2,0), (2,\pm 1), \dots$, the stationary streaks $(0,\pm 1), (0,\pm 2), \dots$, and the MFD $(0,0)$ are also excited.

The amplitude evolution of representative Fourier modes for cases S and P is shown in Figs. 5(a) and 5(c) and Figs. 5(b) and 5(d), respectively. First, the accuracy of the NPSE calculations shown by the solid lines is confirmed by comparing with the DNS results, shown by the dashed lines in Figs. 5(a) and 5(b). Then, for the smooth case, shown in Fig. 5(c), the growth of the 2D fundamental mode $(1,0)$ agrees with the linear prediction (shown by the red circles) until $x \approx 560$, after which it becomes saturated due to nonlinearity. The oblique waves $(1,\pm 1)$ grow at exactly the same rate, and only the amplitude evolution of $(1,1)$ is plotted. It agrees with the linear prediction shown by the pink circles until $x \approx 490$, after which a drastic

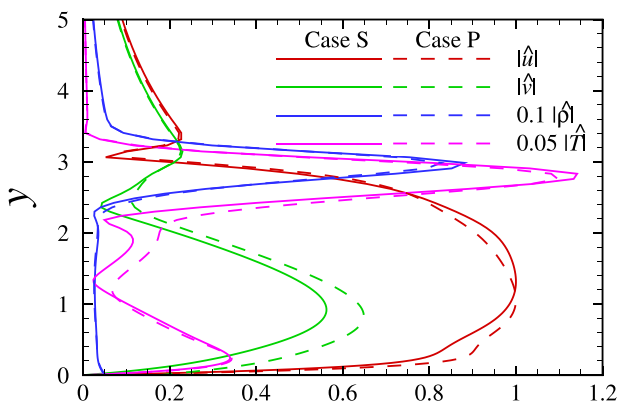


FIG. 4. Eigenfunctions of the 2D Mack second mode for $\omega = 0.6$ at $x = 300$.

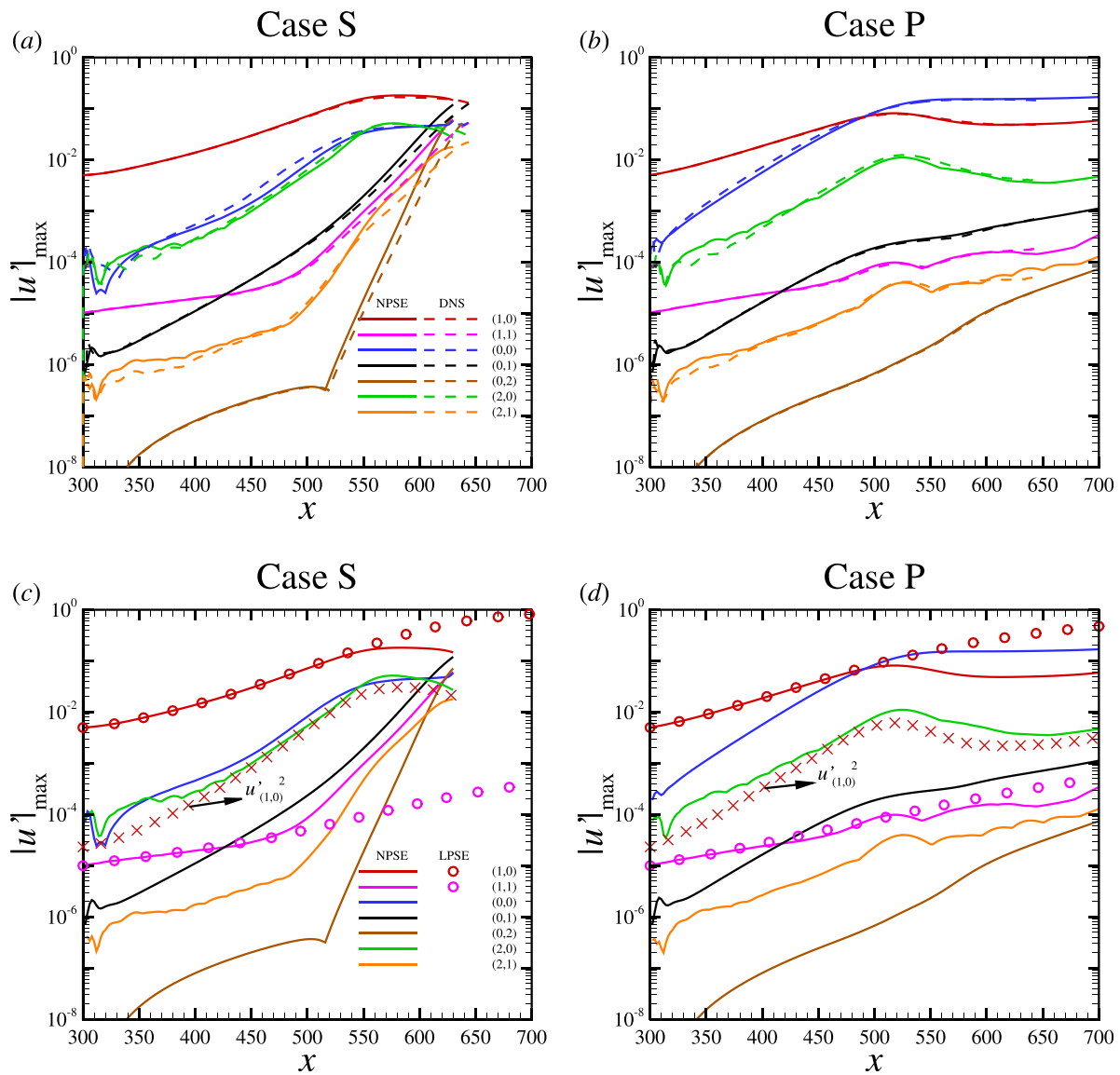


FIG. 5. Streamwise evolution of the u -amplitudes of representative Fourier components. Left column: case S and right column: case P. Top row: comparison between the NPSE and DNS results and bottom row: comparison between the NPSE and LPSE results.

amplification is observed, agreeing with the observations in Ref. 19. This is due to the secondary instability as will be illustrated in Sec. III C 4. The other Fourier components are not seeded at the inlet of the computational domain, but they are excited due to the nonlinear interaction of the introduced perturbations. The MFD (0,0) and the first harmonic of the fundamental mode (2,0) are induced by the self-interaction of the fundamental mode (1,0). Therefore, their amplitudes are almost square of the amplitude of (1,0) in most of the computational domain, as indicated by the red crosses. For $x > 600$, due to the influence of other Fourier components with finite amplitudes, the amplitude of (0,0) becomes much greater than that of (2,0). For $x > 490$, the streak component (0,1) and the high-order harmonics

(2,1) grow at almost the same rate as (1,1), but their amplitudes differ by a certain amount. For $x > 640$, the streak component (0,1) becomes the greatest among these modes, which is the same as the oblique breakdown as in Song *et al.*³⁹ The stronger amplification of the streak mode in the nonlinear phase is attributed to the “lift-up” mechanism. Since the streamwise length scale of the streak mode is much larger than its transverse and lateral length scales, balance of the inertia terms in the momentum equation determines that the amplitude of its streamwise velocity perturbation is much greater than that of its transverse velocity perturbation. The latter is directly driven by the nonlinearity and has an amplitude comparable with component (1,1). Additionally, the streak component (0,2), which is the harmonic of

(0,1), shows an even greater growth rate for $x > 520$, which is twice that of (0,1).

The NPSE calculation for case S blows up at $x = 630$, indicating that the laminar state nearly breaks down and the emergence of turbulence is not far.^{32,33,35} This can also be inferred by observing the coefficient of the surface friction $C_f \equiv 2R^{-1}[\bar{\mu}(\partial\bar{u}/\partial y)]_{y=0}$ and heat flux $q_w \equiv -R^{-1}Pr^{-1}[\bar{\kappa}(\partial\bar{T}/\partial y)]_{y=0}$ as displayed by the red circles in Fig. 6, where the overbar denotes the time- and spanwise-averaging, and κ represents the dimensionless heat conductivity. Both the C_f and q_w curves for case S start from the laminar phase in the upstream locations [shown by the dot-dashed line in Fig. 6(a)] and undergo a remarkable increase from $x \approx 450$, indicating a moderate MFD appearing there. Both curves reach their first peaks at $x \approx 560$, and after a mild decrease, they show rather sharp increases until the blowup position. The double-increase phenomenon is typical for the fundamental resonance, as also reported by a few previous works.^{41,42} The first increase is associated with the saturation of the fundamental mode, while the second increase is attributed to the secondary instability supported by the 2D wavy base flow. For comparison, we also carry out an NPSE calculation by only introducing the 2D fundamental mode as the inflow perturbation (marked by case S_2D), and the results are shown by the red solid lines in Fig. 6. The curves agree with the fundamental resonance results before $x = 600$. Because the 3D perturbations are absent, the second rise in the C_f curve is not seen, and the calculation does not blow up, confirming the role of the 3D perturbations in the late phase of the nonlinear transition process.

For case P, as shown in Fig. 5(d), the amplitude evolution shows three distinguished features. First, the amplitude of the MFD (0,0) is much greater for case P, and its amplification rate cannot be predicted by twice the growth of (1,0) as for case S. Second, the fundamental mode deviates from the linear amplification earlier ($x \approx 490$) due to the greater MFD, and the amplitude of mode (1,0) in the nonlinear saturation state is smaller than that for case S. Third, the growth rates of the secondary instability modes [including (0,1), (1,1), and (2,1)] are much smaller for case P. As a consequence, the calculation for case

P does not blow up even until $x = 700$, as shown in Fig. 6, the results for the calculations with (blue circles) and without (blue solid lines) 3D perturbations agree throughout the computational domain, indicating a significant delay of the transition onset by the porous coating. These three features are to be explained in Subsections III C 2–III C 4.

2. Stronger amplification of the MFD for case P

As indicated in Figs. 5(a) and 5(c), the amplitude of the MFD for case S is well predicted by twice of the $|\tilde{u}_{1,0}|$ -amplitude; however, the MFD for case P undergoes a stronger amplification, as shown in Figs. 5(b) and 5(d). To explain this phenomenon, we compare the perturbation profiles of (1,0) and (0,0) for the two cases in Figs. 7(a) and 7(b), respectively. As shown in Fig. 7(a), although the $|\tilde{u}_{1,0}|$ -amplitude for case P in the late phase ($x \geq 600$) is smaller than that for case S, the shapes of the profiles for the two cases are quite similar, i.e., $|\tilde{u}_{1,0}|$ shows a peak at $y \approx 0.6$ for each case. According to the high- R asymptotic analysis,^{3,4} we know that the Mack mode shows a double-deck structure in the transverse direction, i.e., a main layer where $y = O(\delta)$ and a Stokes layer where $y = O(R^{-1/2}\delta)$, where δ measures the characteristic boundary-layer thickness, and R is the Reynolds number based on δ . A critical layer may appear when the linear mode is nearly neutral. However, since for the present configuration, the Mack growth rate is not very small, the critical layer is not obvious in the plot of $|\tilde{u}_{1,0}|$.

As shown in Fig. 7(b), the shapes of the MFD for cases S and P are quite different. The amplitude of $|\tilde{u}_{0,0}|$ for case P is much greater than that for case S. These differences must be attributed to the admittance boundary condition employed at the wall. However, the mechanism is not obvious since the MFD with a zero frequency is not affected by the admittance boundary condition directly.

Now, let us carry out a simple asymptotic analysis. For simplicity, the analysis is performed in the early nonlinear phase, where the fundamental mode grows almost linearly before reaching the saturation state. As shown in Fig. 5, such a condition is satisfied when $x < 560$ for

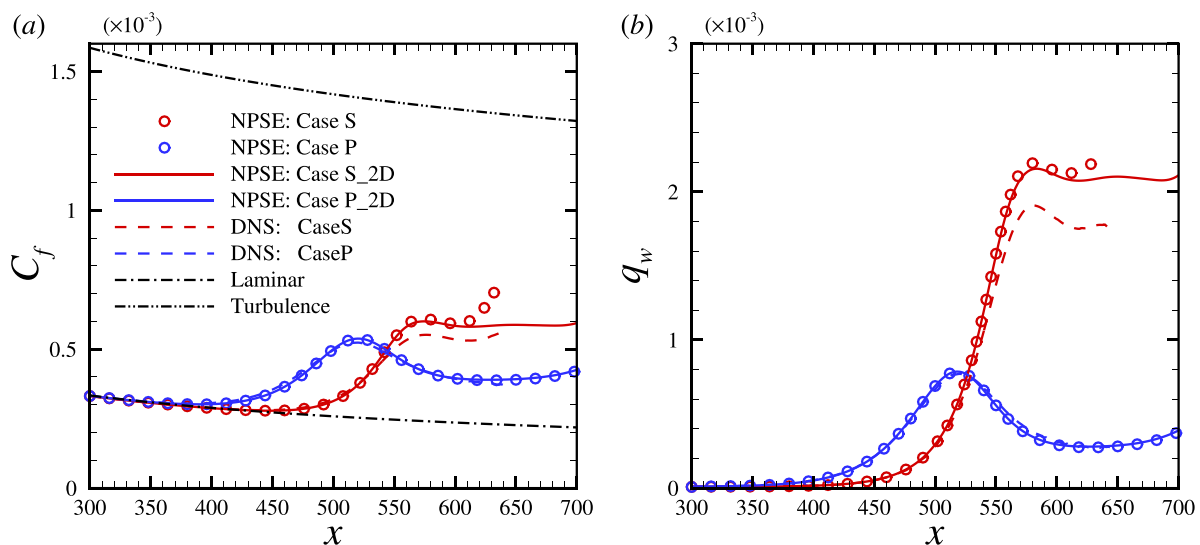
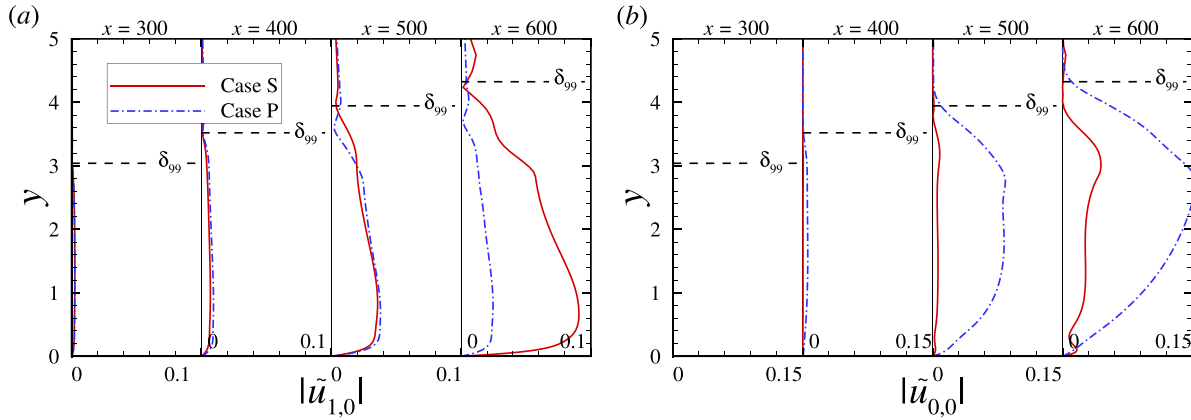


FIG. 6. Streamwise evolution of the C_f (a) and q_w (b) curves. The empirical predictions of C_f for the laminar and turbulent states are from Ref. 40.


 FIG. 7. Eigenfunctions of $|\tilde{u}_{1,0}|$ (a) and $|\tilde{u}_{0,0}|$ (b) for cases S and P.

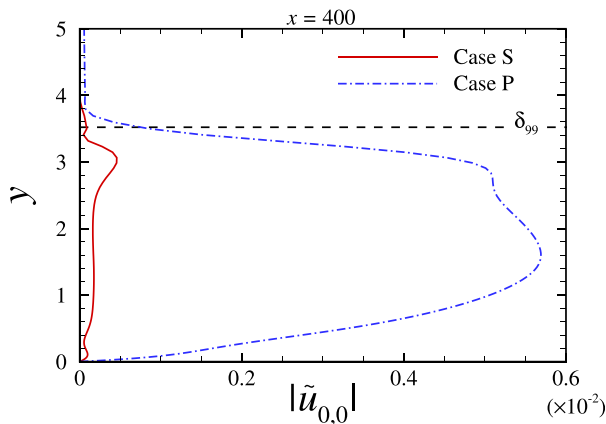
case S and $x < 490$ for case P. The $|\tilde{u}_{0,0}|$ -profiles at $x = 400$ are compared in Fig. 8. The peak of $|\tilde{u}_{0,0}|$ for case S is close to the boundary-layer edge, while $|\tilde{u}_{0,0}|$ for case P shows a double-peak feature, and the lower peak is greater.

In the main layer, we denote the 2D fundamental Mack mode and the MFD by

$$\tilde{\phi}_{1,0}^{S,P} = \mathcal{E}_1 \hat{\phi}_1^{S,P}(y; x) e^{i(\alpha^{S,P}x - \omega t)}, \quad (21)$$

$$\tilde{\phi}_{0,0}^{S,P} = \mathcal{E}_0^2 \hat{\phi}_0^{S,P}(y; x) e^{\sigma^{S,P}x}, \quad (22)$$

respectively, where $\mathcal{E}_1 \ll 1$ measures the amplitude of the fundamental mode, the superscripts S and P denote cases S and P, respectively, $\hat{\phi}_1 \equiv (\hat{u}_1, \hat{v}_1, \hat{p}_1, \hat{\rho}_1, \hat{T}_1)$, $\hat{\phi}_0 \equiv (\hat{u}_0, \hat{v}_0, \hat{p}_0, \hat{\rho}_0, \hat{T}_0)$, and $\alpha^{S,P}$ vary slowly with x , and $\sigma^{S,P} = -2\alpha_i^{S,P} \ll 1$. (In the present calculation, the boundary-layer thickness is $O(1)$, and (α^S, σ^S) and (α^P, σ^P) are quite close.) $\hat{\phi}_1^{S,P}$ to leading order satisfies the Rayleigh equation,^{3,4} and the attenuation condition is applied for both cases S and P. The non-penetration condition is applied at the wall for case S, while according to Eq. (6), the wall boundary condition for case P is $\hat{v}_1^P = A_y \hat{p}_1^P$.


 FIG. 8. Comparison of the $|\tilde{u}_{0,0}|$ for $x = 400$ between cases S and P.

Since $\sigma^{S,P} \ll 1$, balance of the momentum and continuity equations leads to the following scaling estimate:

$$\hat{u}_0^{S,P} \sim (\sigma^{S,P})^{-1}, \quad (\hat{v}_0^{S,P}, \hat{p}_0^{S,P}) \sim 1. \quad (23)$$

Thus, we introduce $\tilde{u}_0^{S,P} = \sigma^{S,P} \hat{u}_0^{S,P}$, and the governing equations to leading order reduce to

$$T_B^{-1} \left(U_B \tilde{u}_0^{S,P} + \frac{dU_B}{dy} \hat{v}_0^{S,P} \right) = F_{10}^{S,P}, \quad (24)$$

$$\frac{d\hat{p}_0^{S,P}}{dy} = F_{20}^{S,P}, \quad (25)$$

$$\tilde{u}_0^{S,P} + \frac{d\hat{v}_0^{S,P}}{dy} = F_{30}^{S,P}, \quad (26)$$

where the inhomogeneous forcing terms are

$$F_{10}^{S,P} = -(\hat{\rho}_1^{S,P})^\dagger \left(S_0^{S,P} \hat{u}_1^{S,P} + \frac{dU_B}{dy} \hat{v}_1^{S,P} \right) - T_B^{-1} \left[(i\alpha^{S,P})(\hat{u}_1^{S,P})^\dagger \hat{u}_1^{S,P} + (\hat{v}_1^{S,P})^\dagger \frac{d\hat{u}_1^{S,P}}{dy} \right] + \text{c.c.}, \quad (27)$$

$$F_{20}^{S,P} = -(\hat{\rho}_1^{S,P})^\dagger S_0^{S,P} \hat{v}_1^{S,P} - T_B^{-1} \left[(i\alpha^{S,P})(\hat{u}_1^{S,P})^\dagger \hat{v}_1^{S,P} + (\hat{v}_1^{S,P})^\dagger \frac{d\hat{v}_1^{S,P}}{dy} \right] + \text{c.c.}, \quad (28)$$

$$F_{30}^{S,P} = -T_B \left\{ (\hat{\rho}_1^{S,P})^\dagger \left[(i\alpha^{S,P}) \hat{u}_1^{S,P} + \frac{d\hat{v}_1^{S,P}}{dy} \right] + (i\alpha^{S,P})(\hat{u}_1^{S,P})^\dagger \hat{\rho}_1^{S,P} + (\hat{v}_1^{S,P})^\dagger \frac{d\hat{\rho}_1^{S,P}}{dy} \right\} + (\hat{T}_1^{S,P})^\dagger S_0^{S,P} \hat{\rho}_1^{S,P} - (\hat{\rho}_1^{S,P})^\dagger \frac{dT_B}{dy} \hat{v}_1^{S,P} + (\gamma - 1)M^2 \left[(i\alpha^{S,P})(\hat{u}_1^{S,P})^\dagger \hat{p}_1^{S,P} + (\hat{v}_1^{S,P})^\dagger \frac{d\hat{p}_1^{S,P}}{dy} \right] - T_B^{-1} \left[(i\alpha^{S,P})(\hat{u}_1^{S,P})^\dagger \hat{T}_1^{S,P} + (\hat{v}_1^{S,P})^\dagger \frac{d\hat{T}_1^{S,P}}{dy} \right] + \text{c.c.}, \quad (29)$$

with $S_0^{S,P} = i(\alpha^{S,P}U_B - \omega)$, and the superscript “†” denotes the complex conjugate. Here, Eq. (25) is obtained by inserting the energy equation into the continuity equation, such that the density and temperature of the mean-flow distortion are eliminated.

Solving Eqs. (24) to (26), we obtain

$$\hat{v}_0^{S,P} = U_B \left(\int_{a^{S,P}}^y H_0^{S,P} dy + b^{S,P} \right), \tag{30}$$

$$\tilde{u}_0^{S,P} = \frac{T_B F_{10}^{S,P} - \frac{dU_B}{dy} \hat{v}_0^{S,P}}{U_B}, \tag{31}$$

where

$$H_0^{S,P} = \frac{F_{30}^{S,P} - T_B F_{10}^{S,P} / U_B}{U_B}, \tag{32}$$

and $a^{S,P}$ and $b^{S,P}$ are constants to be determined by the wall boundary conditions.

For a smooth wall, where $\hat{v}_1^S(0) = 0$, applying the Rayleigh equations for the fundamental mode at the wall leads to

$$\hat{u}_1^S \rightarrow \left[\frac{\alpha^S}{\omega} T_w + \left(\frac{\alpha^S}{\omega} \lambda_T + \lambda M^2 \right) y + O(y^2) \right] \hat{p}_1^S(0),$$

$$\hat{v}_1^S \rightarrow i \left[\omega M^2 - \frac{(\alpha^S)^2}{\omega} T_w \right] y \hat{p}_1^S(0) + O(y^2),$$

$$\hat{\rho}_1^S \rightarrow \left\{ \frac{M^2}{T_w} + \left[\frac{-2M^2}{T_w^2} + \frac{(\alpha^S)^2}{T_w \omega^2} \right] \lambda_T y + O(y^2) \right\} \hat{p}_1^S(0), \tag{33}$$

$$\hat{T}_1^S \rightarrow \left\{ (\gamma - 1) M^2 T_w + \left[\gamma M^2 - \frac{T_w (\alpha^S)^2}{\omega^2} \right] \lambda_T y + O(y^2) \right\} \hat{p}_1^S(0),$$

as $y \rightarrow 0$, where $\lambda = (dU_B/dy)_{y=0}$ and $\lambda_T = (dT_B/dy)_{y=0}$. Here, $\hat{p}_1^S(0)$ is taken to be unity for normalization, and $(d\hat{p}_1^{S,P}/dy)_{y=0} = 0$. Since $\sigma^S \ll \alpha_r^S$, we can take α^S to leading order to be real, and the inhomogeneous forcing terms in the near wall region behave as

$$F_{10}^S \rightarrow O(y^2), \quad F_{30}^S \rightarrow O(y^2) \quad \text{as } y \rightarrow 0. \tag{34}$$

Thus, $H_0^S \rightarrow 0$ as $y \rightarrow 0$. Considering the non-penetration boundary condition at the wall, we simply take $a^S = 0$ and $b^S = 0$. The no-slip boundary condition is automatically satisfied.

However, for a porous wall, for which $\hat{v}_1^P(0) = A_y \hat{p}_1^P(0)$, we find that

$$(F_{10}^P, F_{30}^P) \rightarrow O(1) \quad \text{as } y \rightarrow 0. \tag{35}$$

Then, as $y \rightarrow 0$, $H_0^P \rightarrow O(y^{-2})$, and

$$\hat{v}_0^P \rightarrow \frac{T_w F_{10}^P(0)}{\lambda} + F_{30}^P(0) y \ln y + \dots, \tag{36}$$

$$\tilde{u}_0^P \rightarrow -F_{30}^P(0) \ln y + \dots. \tag{37}$$

It is seen that the perturbation velocity field is singular at the wall. To remove the singularity, the viscosity has to be taken into account in a thin layer near the wall. Balancing the convection terms with the viscous terms in the momentum equation, we obtain

$$\sigma U_B \hat{u}_0^P \sim \sigma \lambda y \hat{u}_0^P \sim R^{-1} d^2 \hat{u}_0^P / dy^2, \tag{38}$$

which leads to $y \sim (\sigma R)^{-1/3}$. This indicates that the thickness of the viscous wall layer is $\delta_v = O((\sigma R)^{-1/3})$. The solution of \hat{u}_0^P should be an integral of the Airy function, which is similar to the wall-layer solution in Dong *et al.*³

In fact, we do not need to show the detailed mathematics for the wall-layer solution here. The most important observation is that the leading-order solution of the MFD for case S satisfies the no-slip and non-penetration boundary conditions without any singularity; however, the MFD for case P shows a logarithmic singular as the wall is approached. This answers why the admittance condition could have a severe impact on the steady MFD. Additionally, the lower peak of $|\tilde{u}_{0,0}|$ for case P is related to the wall-layer solution.

The above analysis reveals the mechanism that the MFD for case P undergoes a stronger amplification before the fundamental mode reaches its saturation state. Although at further downstream locations, such an analysis is not rigorously valid, because the feedback of the MFD and harmonics to the fundamental mode must be considered there (the nonlinear-critical-layer analysis as in Ref. 43 may be an appropriate tool), we may expect a similar mechanism for the stronger amplification of the MFD there. It is seen from Fig. 7(b) that for $x = 600$, the double-peak feature of $|\tilde{u}_{0,0}|$ is replaced by one single peak, but the peak value for case P is much greater than that for case S.

3. Greater suppression of the fundamental modes by the MFD for case P

As shown by the red lines in Fig. 5, the growth rate of the 2D fundamental mode in the nonlinear phase becomes smaller than the linear prediction, because the mean flow is severely distorted by the (0,0) component. To quantify this, we perform the linear stability analysis based on the distorted mean flow $\bar{\Phi}$, including Φ_B and the MFD, for two representative streamwise positions, which is compared to the LST results based on Φ_B , as shown in Fig. 9. For both cases S and P, the growth rates based on $\bar{\Phi}$ are smaller than those based on Φ_B for the considered frequencies, indicating a suppression effect of the MFD on the fundamental mode. This suppression effect is greater for case P, implying that the fundamental mode for case P is likely to accumulate to a lower saturated amplitude. A further comparison of the amplitudes obtained by LST based on Φ_B and $\bar{\Phi}$ is shown in Fig. 10. For both cases, the LST predictions based on Φ_B agree overall with the LPSE calculations, while the LST predictions based on $\bar{\Phi}$ agree overall with the NPSE calculation until the blowup position ($x = 630$). This confirms the reliability of the method that explains the suppression effect of the MFD by linear stability analysis. For case S, the agreement of the LST and PSE results is not as good as that for case P, indicating that a stronger non-parallelism appears for this case.

In Fig. 11, we show the NPSE calculations of the amplitude evolution for each Fourier component by removing artificially the MFD for the two cases, which are compared with the original NPSE calculations. For case S, shown in Fig. 11(a), the difference between the two families of curves is rather limited. The only difference is that the blowup position for the calculation without the MFD shifts upstream slightly, namely, from $x = 630$ to $x = 616$. For case P, as shown in Fig. 11(b), when the MFD is absent, the fundamental mode saturates at a higher amplitude, and the calculation blows up at $x \approx 644$. The implication is that the enhanced MFD by the porous wall plays a significant suppression effect on the 2D fundamental mode, and the blowup of the NPSE calculation without MFD is attributed to the secondary

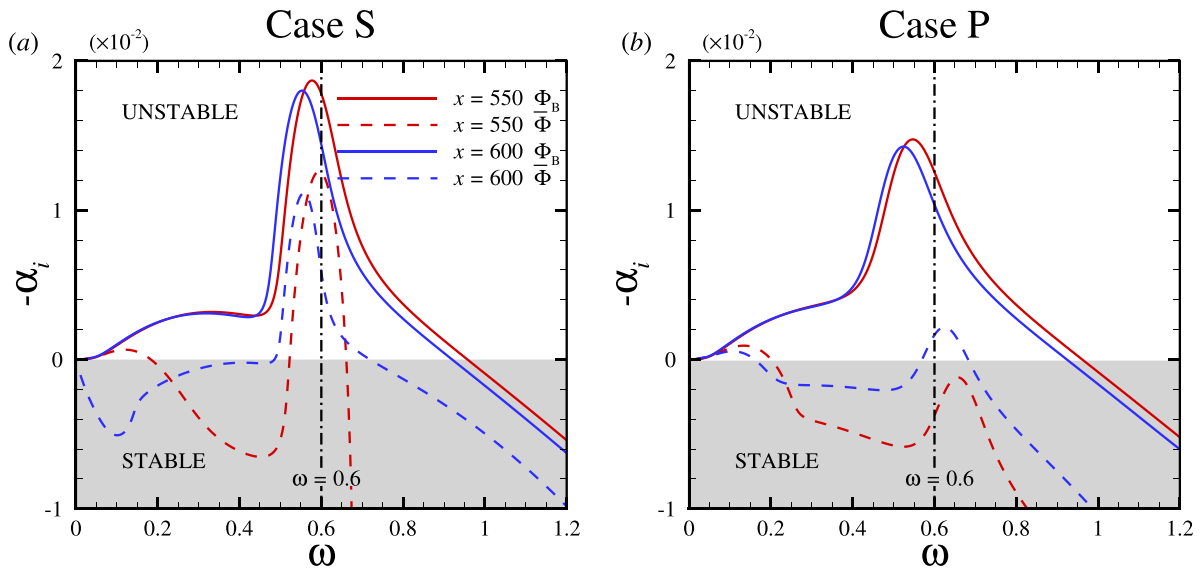


FIG. 9. Comparison of the LST predictions of the Mack-mode growth rates based on $\bar{\Phi}$ and Φ_B : (a) case S and (b) case P.

instability supported by the fundamental mode with a higher amplitude.

4. Secondary instability analysis (SIA)

When the 2D fundamental mode for case S or case P reaches a finite amplitude, the secondary instability modes are likely to be amplified rapidly due to the fundamental resonance, as studied previously based on the Floquet theory.^{41,42,44} Taking the frequency and wavenumber of the 2D fundamental mode to be ω and α_r , the base flow

$\check{\phi}_B$ for the Floquet analysis consists of the Blasius base flow in a moving frame and the Fourier transformed perturbations,

$$\check{\phi}_B(\tilde{x}, y) = [\rho_B, U_B - c, 0, 0, T_B](y) + \sum_{m=-M_S}^{M_S} \tilde{\epsilon}_{m,0} \tilde{\phi}_{m,0}(y) e^{im\alpha_r \tilde{x}}, \tag{39}$$

where the Galilean transformation $\tilde{x} = x - ct$ is introduced to remove the time-dependent terms, with $c = \omega/\alpha_r$ denoting the phase speed of the 2D fundamental mode. M_S is the truncation order of the Fourier

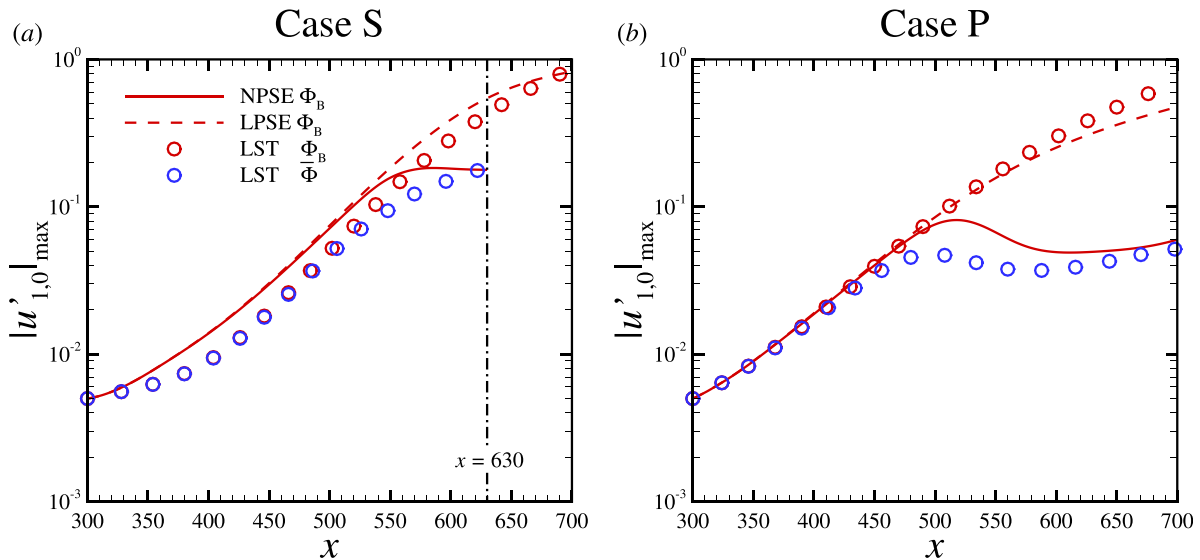


FIG. 10. Streamwise evolution of the $|u'|_{\max}$ amplitude for the fundamental mode (1,0): (a) case S and (b) case P.

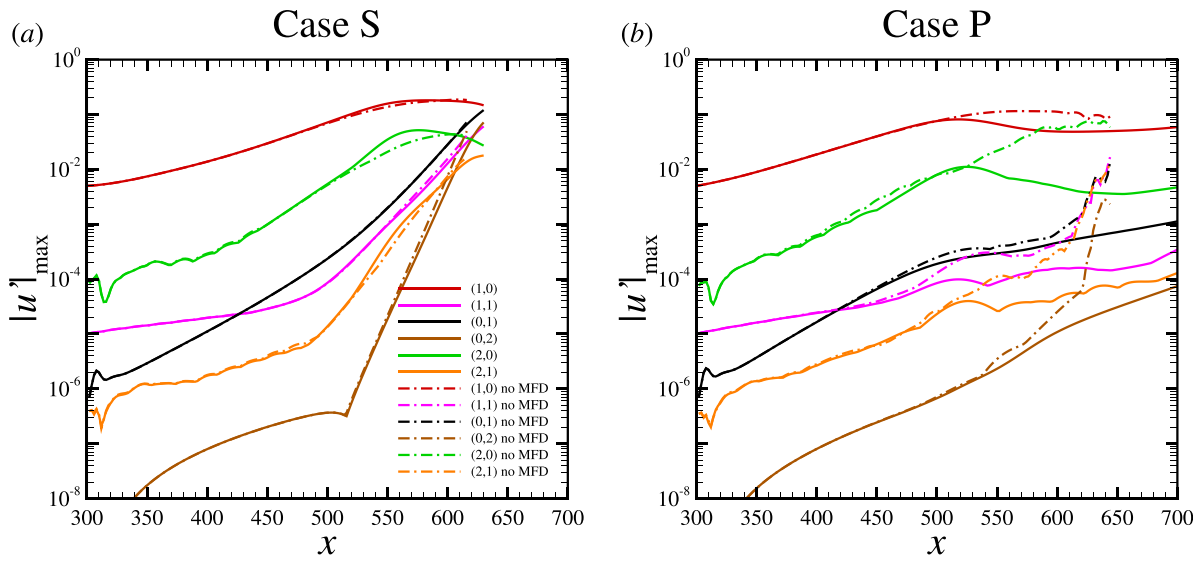


FIG. 11. Comparison of the streamwise evolution of the \tilde{u} -amplitude between the NPSE calculations (solid lines) and those by removing artificially the MFD (dashed lines): (a) case S and (b) case P.

series, and $\tilde{\epsilon}_{m,0}$ and $\tilde{\phi}_{m,0} \equiv (\tilde{\rho}_{m,0}, \tilde{u}_{m,0}, \tilde{v}_{m,0}, \tilde{w}_{m,0}, \tilde{T}_{m,0})$ denote the amplitude and shape function of each 2D Fourier component obtained by NPSE calculations, respectively. Here, the growth of the fundamental mode is neglected because $|\alpha_i| \ll \alpha_r$.

According to the Floquet theory, the secondary instability mode can be given by

$$\begin{aligned} \phi'_S(\tilde{x}, y, z, t) &= \bar{\epsilon} e^{i[\gamma(\tilde{x}+ct)+\beta z]} e^{i\sigma_d \alpha_r \tilde{x}} \tilde{\phi}_S(\tilde{x}, y) + c.c., \\ \tilde{\phi}_S(\tilde{x}, y) &= \sum_{n=-N_S}^{N_S} \tilde{\phi}_{S,n}(y) e^{in\alpha_r \tilde{x}}, \end{aligned} \quad (40)$$

where $\gamma = \gamma_r + i\gamma_i$ is the complex streamwise wavenumber with $-\gamma_i$ denoting its growth rate. $\bar{\epsilon}$ is the amplitude, β is the spanwise wavenumber, and N_S is the truncation order of the Fourier series. $\sigma_d \in [0, 0.5]$ is a detuning parameter that identifies the distinct resonance stages of the secondary instability, and we take $\sigma_d = 0$ for the fundamental resonance. Substituting Eqs. (39) and (40) in the linearized Navier–Stokes equations and neglecting the non-parallel terms, we arrive at a linear equation system,

$$\left[\mathbf{M}_0 + (i\gamma)\mathbf{M}_1 + (i\gamma)^2\mathbf{M}_2 \right] \tilde{\phi}_S(\tilde{x}, y) = 0, \quad (41)$$

where

$$\begin{aligned} \mathbf{M}_0 &= (\mathbf{A} + i\beta\mathbf{V}_{xz}) \frac{\partial}{\partial \tilde{x}} + (\mathbf{B} + i\beta\mathbf{V}_{yz}) \frac{\partial}{\partial y} \\ &+ [i\beta\mathbf{C} + \mathbf{D} + (i\beta)^2\mathbf{V}_{zz}] + \mathbf{V}_{xx} \frac{\partial^2}{\partial \tilde{x}^2} \\ &+ \mathbf{V}_{yy} \frac{\partial^2}{\partial y^2} + \mathbf{V}_{xy} \frac{\partial^2}{\partial \tilde{x} \partial y}, \\ \mathbf{M}_1 &= (\mathbf{A} + i\beta\mathbf{V}_{xz}) + 2\mathbf{V}_{xx} \frac{\partial}{\partial \tilde{x}} + \mathbf{V}_{xy} \frac{\partial}{\partial y} + c\Gamma, \quad \mathbf{M}_2 = \mathbf{V}_{xx}, \end{aligned} \quad (42)$$

where the coefficient matrices $\mathbf{A}, \mathbf{B}, \mathbf{C}, \mathbf{D}, \Gamma, \mathbf{V}_{xx}, \mathbf{V}_{xy}, \mathbf{V}_{xz}, \mathbf{V}_{yy}, \mathbf{V}_{yz}, \mathbf{V}_{zz}$ can be found in Ref. 23. The boundary conditions are the same as Eqs. (12) and (13) for a porous wall or Eqs. (12) and (14) for a smooth wall. Again, the system [Eq. (41)] with the homogeneous boundary conditions forms an eigenvalue problem with γ appearing as the eigenvalue, and the same numerical approach as in Eq. (11) is employed. The code validation is provided in Appendix B.

Performing the SIA for $x > 500$, we calculate the growth rate $-\gamma_i$ of the secondary instability mode for $\beta = 0.4$ at each position. Integrating these growth rates along x , we obtain the accumulated amplitude of the secondary instability modes, as shown by the crosses in Fig. 12. The growth rates for both cases S and P agree with the NPSE calculations of modes (0,1), (1,1), and (2,1). Figure 13 compares the eigen-profiles of the Fourier components (0,1) and (1,1) obtained by NPSE and SIA at $x = 550$. The agreement for case S is perfect, but a small discrepancy between the NPSE and SIA results is observed for case P. The reason is that since the amplification of the secondary instability mode for case P is weaker, the contributions by other factors, such as the nonlinearity, are not negligible. The growth rate for case P is much lower than that for case S, because the amplitude of the saturated fundamental mode is smaller for case P. This implies that the transition occurs later for case P.

IV. CONCLUSIONS

In this paper, we study the nonlinear evolution of the Mack modes over a hypersonic boundary layer coated by a porous wall by the use of the NPSE approach. To quantify the impact of the porous effect, a calculation over a smooth wall is also conducted for comparison. The inflow perturbations are selected to include a finite-amplitude 2D Mack mode and a pair of small-amplitude 3D Mack modes with the same frequency as

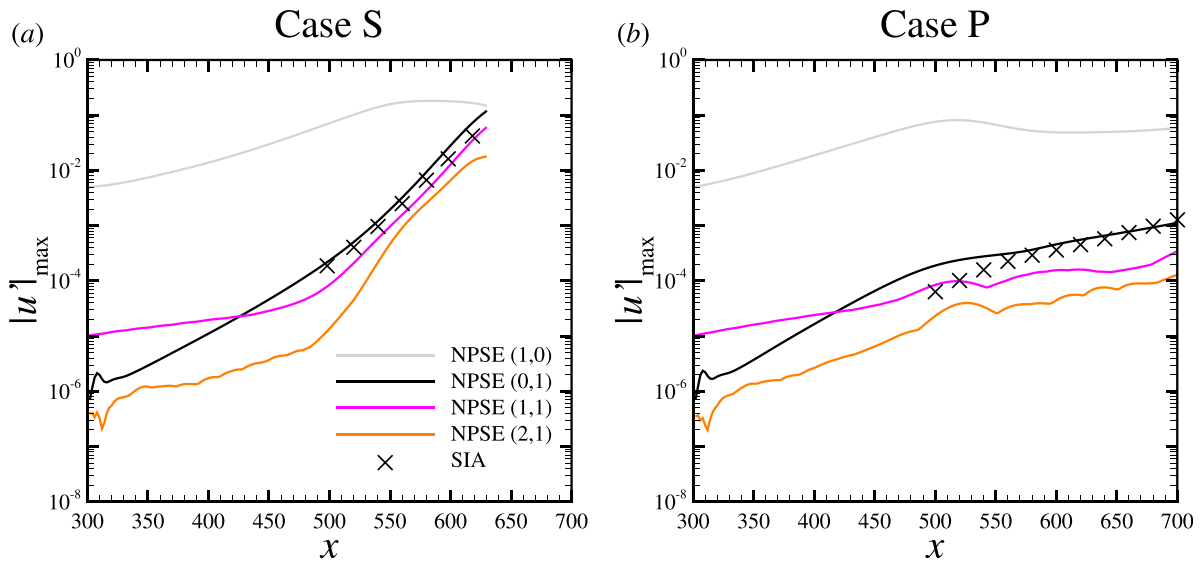


FIG. 12. Comparison of the amplitudes of modes (0,1), (1,1), and (2,1) with the SIA predictions: (a) case S and (b) case P.

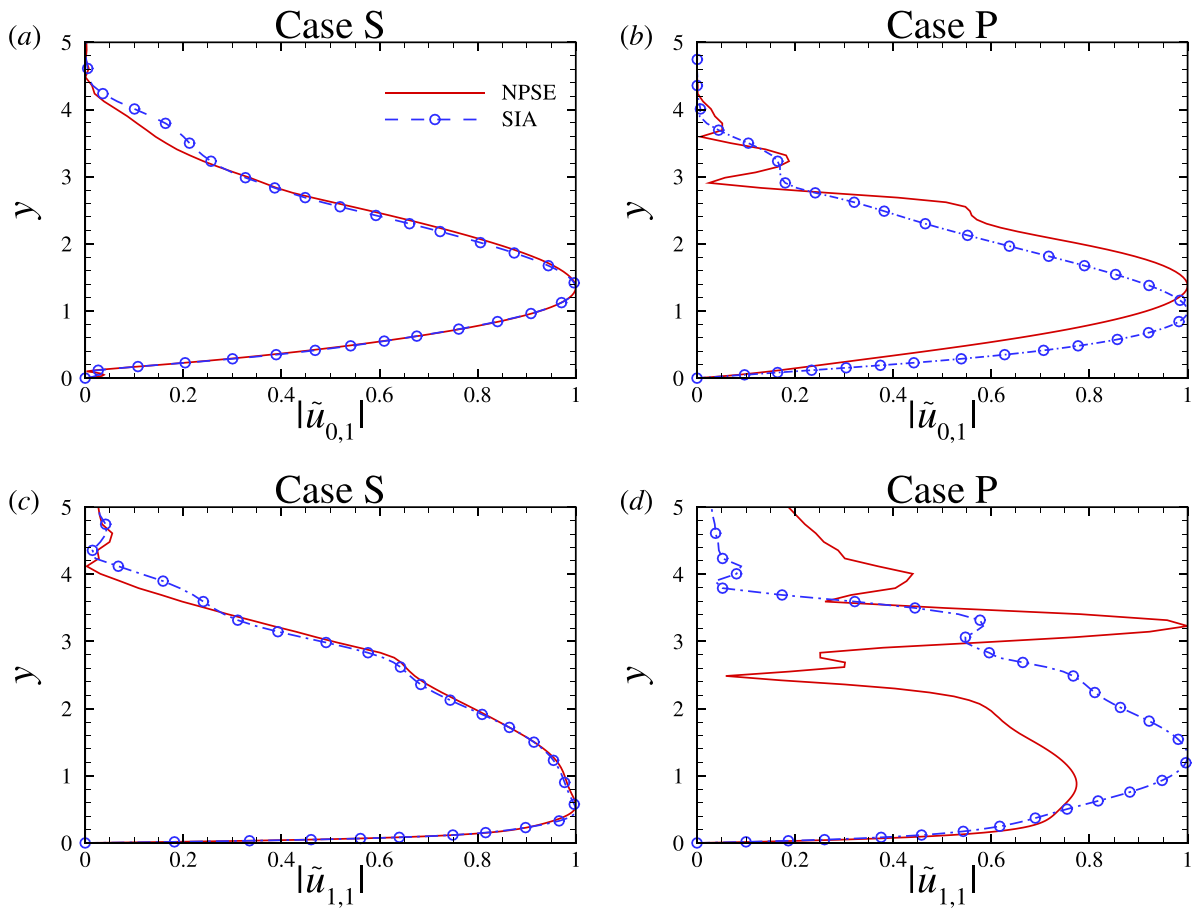


FIG. 13. Normalized eigen-profiles of $|\tilde{u}_{0,1}|$ (top row) and $|\tilde{u}_{1,1}|$ (bottom row) obtained by NPSE and SIA. Left column: case S and right column: case P.

the 2D mode but opposite spanwise wavenumbers. These perturbations satisfy the fundamental resonance, which is found to be a rather efficient means to trigger transition to turbulence in hypersonic boundary layers. The NPSE calculations are confirmed to be sufficiently accurate in comparison with the DNS results.

For both the smooth and porous cases, the evolution of each Fourier component follows overall the same feature. The 2D fundamental mode grows exponentially in the early laminar phase; when the mean-flow distortion driven by the self-interaction of the fundamental mode reaches a high level, it can act back on the fundamental mode and lead to the nonlinear saturation of the latter; meanwhile, the streak mode and high-order harmonics grow under the secondary instability. However, three distinguished features are highlighted and explained in detail.

- (1) When the amplitude of the fundamental mode reaches a finite level, the amplification of the MFD for case P is remarkably greater than that for case S. An asymptotic analysis is performed to explain this phenomenon by considering the main-layer response of the MFD to the self-interaction of the fundamental mode. For case S, the solution is regular and peaks near the boundary-layer edge, whereas for case P, the solution shows a logarithmic singularity near the wall, and an additional viscous wall layer appears. This singularity ensures a much greater amplitude of the MFD for case P.
- (2) In the nonlinear phase, the fundamental mode undergoes a reduction in its growth rate, which can be predicted overall by analyzing the linear instability property based on the time-averaged mean flow consisting of the base flow and the MFD. The implication is that the presence of the MFD plays a stabilizing role on the development of the fundamental mode. Since the MFD for case P is greater, the corresponding saturated amplitude of the fundamental mode is smaller due to the stronger suppression effect.
- (3) When the fundamental mode reaches a sufficiently high amplitude, the Fourier components with the same spanwise wavenumber, namely, (0,1), (1,1), (2,1), \dots , are amplified rapidly due to the secondary instability, which is confirmed by comparing the growth rates and the eigen-profiles between the NPSE and SIA results. For case P, since the saturated amplitude of the fundamental mode is lower, the growth rate of the secondary instability mode is smaller, leading to a delay in the downstream transition location.

Although the above calculations are based on a particular configuration, the theoretical analysis is quite generic, and so can be applied to more broad cases as long as the fundamental resonance appears. Inspired by the findings of the present work, one may evaluate the laminar-flow control strategy by applying the porous section in a more efficient way. Since the porous effect could suppress the saturation amplitude of the fundamental 2D mode, the nonlinear phase can be lengthened remarkably. Therefore, the equivalent transition threshold for the e-N transition prediction method should be increased to compensate the lengthened nonlinear phase. Also, the analytical model in Sec. III C 2 provides a means to obtain quantitatively the mean-flow distortion induced by the nonlinearity of the fundamental

mode, which can be used to evaluate the increment in the transition threshold due to the porous effect. Admittedly, the fundamental resonance is not the only nonlinear regime in the transition process of hypersonic boundary layers, and the porous effect on the nonlinear Mack modes under other nonlinear regimes is also an attractive issue and worth to be done in the future.

ACKNOWLEDGMENTS

This research was supported by the NSFC (Grant Nos. U20B2003, 12002235, and 11988102).

AUTHOR DECLARATIONS

Conflict of Interest

The authors have no conflicts to disclose.

Author Contributions

Qinyang Song: Data curation (lead); Formal analysis (equal); Investigation (equal); Validation (equal); Writing – original draft (equal). **Lei Zhao:** Conceptualization (equal); Funding acquisition (equal); Investigation (equal); Methodology (lead); Resources (equal); Software (lead); Supervision (equal). **Ming Dong:** Conceptualization (equal); Formal analysis (lead); Funding acquisition (equal); Project administration (lead); Resources (equal); Supervision (equal); Writing – review & editing (lead).

DATA AVAILABILITY

The data that support the findings of this study are available from the corresponding authors upon reasonable request.

APPENDIX A: RESOLUTION TESTS FOR THE NPSE CALCULATION

The NPSE resolution tests for cases S and P are shown in Fig. 14, where the computational configurations are the same as that in Fig. 5. The present results for the standard mesh agree well with those obtained by increasing the x -direction grid points to 251 and increasing the y -direction grid points to 301, separately, confirming the reliability of the calculations in the current paper.

APPENDIX B: VALIDATION OF THE SIA CODE

To verify our SIA code, we perform calculations for the sub-harmonic resonance as studied in Ng and Erlebacher.⁴⁵ The physical model is a Mach-4.5 boundary layer over an adiabatic flat plate, where $R = 1 \times 10^4$ (R is the Reynolds number based on the boundary-layer displacement thickness), and $T_\infty^* = 61.11$ K. The fundamental mode is a 2D Mack mode with $\alpha = 2.52$, and the temporal SIA is performed for three amplitudes of the 2D mode, namely, $\varepsilon = 0.02, 0.03, \text{ and } 0.06$. As shown in Fig. 15, our calculations agree perfectly with the results in Ref. 45, confirming the reliability of our SIA code.

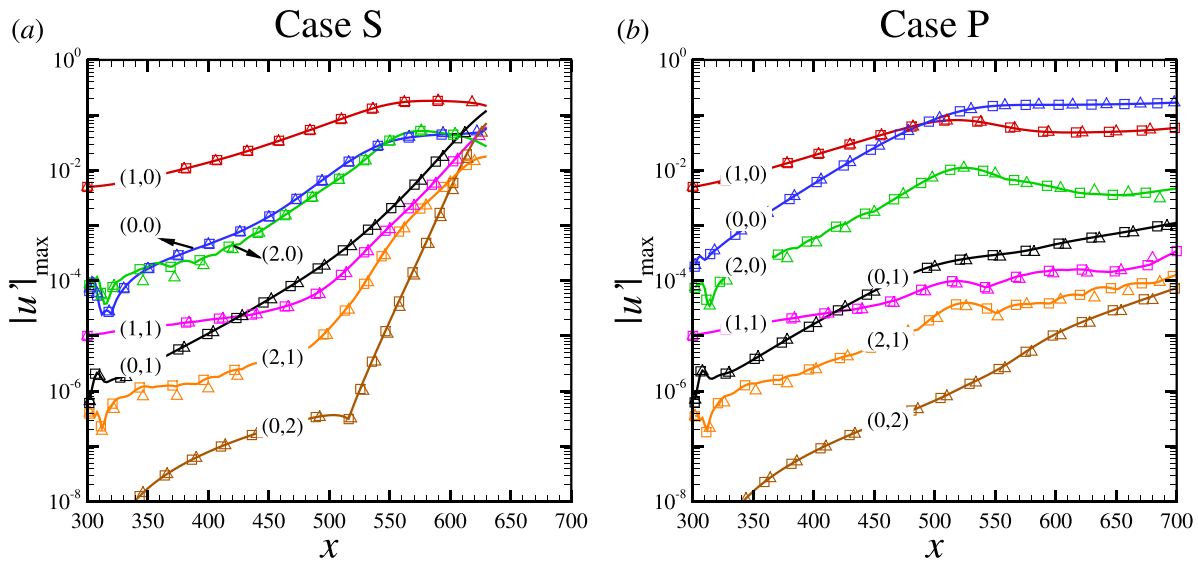


FIG. 14. Resolution tests for the NPSE calculations obtained by different mesh scales, where the solid lines are for the standard mesh, the square symbols are for the mesh refined in the x direction, and the triangle symbols are for the mesh refined in the y direction: (a) case S and (b) case P.

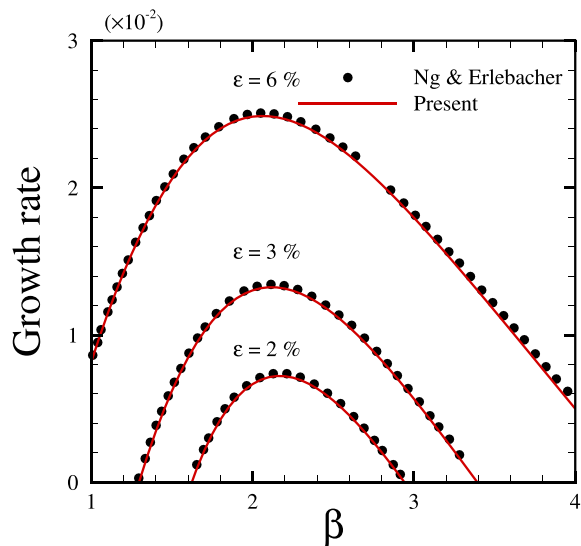


FIG. 15. Comparison of the temporal growth rates of the secondary instability modes between our calculations and the results in Ref. 45.

REFERENCES

¹Y. S. Kachanov, “Physical mechanisms of laminar-boundary-layer transition,” *Annu. Rev. Fluid Mech.* **26**, 411–482 (1994).
²L. M. Mack, “Review of linear compressible stability theory,” in *Stability of Time Dependent and Spatially Varying Flows* (Springer, 1987), pp. 164–187.
³M. Dong, Y. Liu, and X. Wu, “Receptivity of inviscid modes in supersonic boundary layers due to scattering of free-stream sound by localised wall roughness,” *J. Fluid Mech.* **896**, A23 (2020).
⁴M. Dong and L. Zhao, “An asymptotic theory of the roughness impact on inviscid Mack modes in supersonic/hypersonic boundary layers,” *J. Fluid Mech.* **913**, A22 (2021).

⁵A. V. Fedorov, “Transition and stability of high-speed boundary layers,” *Annu. Rev. Fluid Mech.* **43**, 79–95 (2011).
⁶N. D. Malmuth, A. V. Fedorov, V. Shalaev, J. Cole, M. Hites, and D. Williams, “Problems in high speed flow prediction relevant to control,” AIAA Paper No. 1998-2695, 1998.
⁷A. V. Fedorov, N. D. Malmuth, A. Rasheed, and H. G. Hornung, “Stabilization of hypersonic boundary layers by porous coatings,” *AIAA J.* **39**, 605–610 (2001).
⁸A. V. Fedorov, A. N. Shpilyuk, A. A. Maslov, E. Burov, and N. D. Malmuth, “Stabilization of a hypersonic boundary layer using an ultrasonically absorptive coating,” *J. Fluid Mech.* **479**, 99–124 (2003).
⁹A. V. Fedorov, V. Kozlov, A. N. Shpilyuk, A. A. Maslov, and N. D. Malmuth, “Stability of hypersonic boundary layer on porous wall with regular microstructure,” *AIAA J.* **44**, 1866–1871 (2006).
¹⁰A. V. Fedorov, A. N. Shpilyuk, A. A. Maslov, E. Burov, and N. D. Malmuth, “Stabilization of a hypersonic boundary layer using an ultrasonically absorptive coating—CORRIGENDUM,” *J. Fluid Mech.* **769**, 725–728 (2015).
¹¹V. C. B. Sousa, D. Patel, J. B. Chapelier, V. Wartemann, A. Wagner, and C. Scalò, “Numerical investigation of second-mode attenuation over carbon/carbon porous surfaces,” *J. Spacecr. Rockets* **56**, 319–332 (2019).
¹²R. Fiévet, H. Deniau, J.-P. Brazier, and E. Piot, “Numerical analysis of porous coatings stabilizing capabilities on hypersonic boundary-layer transition,” *AIAA J.* **59**, 3845–3858 (2021).
¹³A. A. Maslov, A. N. Shpilyuk, A. Sidorenko, P. Polivanov, A. V. Fedorov, V. Kozlov, and N. D. Malmuth, “Hypersonic laminar flow control using a porous coating of random microstructure,” AIAA Paper No. 2006-1112, 2006.
¹⁴V. Wartemann, A. Wagner, M. Kuhn, T. Eggers, and K. Hannemann, “Passive hypersonic boundary layer transition control using an ultrasonically absorptive coating with random microstructure: Computational analysis based on the ultrasonic absorption properties of carbon-carbon,” *Procedia IUTAM* **14**, 413–422 (2015).
¹⁵S. A. Miller, J. J. Redmond, K. Jantze, C. Scalò, and J. S. Jewell, “Investigation of second-mode instability attenuation over porous materials in Mach-6 quiet flow,” AIAA Paper No. 2022-3530, 2022.
¹⁶Q. Song and L. Zhao, “Scattering of Mack modes by solid-porous junctions in hypersonic boundary layers,” *Phys. Fluids* **34**, 084104 (2022).
¹⁷Y. Liu, M. Dong, and X. Wu, “Generation of first Mack modes in supersonic boundary layers by slow acoustic waves interacting with streamwise isolated wall roughness,” *J. Fluid Mech.* **888**, A10 (2020).

08 April 2024 03:12:44

- ¹⁸X. Wu, “Nonlinear theories for shear flow instabilities: Physical insights and practical implications,” *Annu. Rev. Fluid Mech.* **51**, 451–485 (2019).
- ¹⁹X. Wu, J. Luo, and Y. Ming, “Transition route of Klebanoff type in hypersonic boundary layers,” AIAA Paper No. 2016-3953, 2016.
- ²⁰N. Chokani, D. A. Bountin, A. N. Shplyuk, and A. A. Maslov, “Nonlinear aspects of hypersonic boundary-layer stability on a porous surface,” *AIAA J.* **43**, 149–155 (2005).
- ²¹W. Zhu, M. Shi, Y. Zhu, and C. Lee, “Experimental study of hypersonic boundary layer transition on a permeable wall of a flared cone,” *Phys. Fluids* **32**, 011701 (2020).
- ²²W. Zhu, X. Chen, Y. Zhu, and C. Lee, “Nonlinear interactions in the hypersonic boundary layer on the permeable wall,” *Phys. Fluids* **32**, 104110 (2020).
- ²³L. Zhao, M. Dong, and Y. Yang, “Harmonic linearized Navier–Stokes equation on describing the effect of surface roughness on hypersonic boundary-layer transition,” *Phys. Fluids* **31**, 034108 (2019).
- ²⁴L. Zhao and M. Dong, “Effect of suction on laminar-flow control in subsonic boundary layers with forward-/backward-facing steps,” *Phys. Fluids* **32**, 054108 (2020).
- ²⁵L. Zhao and M. Dong, “Effect of surface temperature strips on the evolution of supersonic and hypersonic Mack modes: Asymptotic theory and numerical results,” *Phys. Rev. Fluids* **7**, 053901 (2022).
- ²⁶P. Sun, L. Zhao, and M. Dong, “Study on the evolution of non-modal disturbances in hypersonic boundary layer based on HLNS approach,” *Adv. Mech.* **52**, 180–195 (2022) (in Chinese).
- ²⁷D. L. Johnson, J. Koplik, and R. Dashen, “Theory of dynamic permeability and tortuosity in fluid-saturated porous media,” *J. Fluid Mech.* **176**, 379–402 (1987).
- ²⁸M. R. Malik, “Numerical methods for hypersonic boundary layer stability,” *J. Comput. Phys.* **86**, 376–413 (1990).
- ²⁹X. Wu and M. Dong, “Entrainment of short-wavelength free-stream vortical disturbances in compressible and incompressible boundary layers,” *J. Fluid Mech.* **797**, 683–728 (2016).
- ³⁰A. Fedorov, V. Soudakov, I. Egorov, A. Sidorenko, Y. Gromyko, D. Bountin, P. Polivanov, and A. Maslov, “High-speed boundary-layer stability on a cone with localized wall heating or cooling,” *AIAA J.* **53**, 2512–2524 (2015).
- ³¹F. P. Bertolotti, T. Herbert, and P. R. Spalart, “Linear and nonlinear stability of the Blasius boundary layer,” *J. Fluid Mech.* **242**, 441–474 (1992).
- ³²C.-L. Chang and M. R. Malik, “Oblique-mode breakdown and secondary instability in supersonic boundary layers,” *J. Fluid Mech.* **273**, 323–360 (1994).
- ³³T. Herbert, “Parabolized stability equations,” *Annu. Rev. Fluid Mech.* **29**, 245–283 (1997).
- ³⁴Y. Zhang and H. Zhou, “Verification of parabolized stability equations for its application to compressible boundary layers,” *Appl. Math. Mech.* **28**, 987–998 (2007).
- ³⁵M. Dong, Y. Zhang, and H. Zhou, “A new method for computing laminar-turbulent transition and turbulence in compressible boundary layers–PSE+DNS,” *Appl. Math. Mech.* **29**, 1527–1534 (2008).
- ³⁶C. Zhang and J. Luo, “Selective enhancement of oblique waves caused by finite amplitude second mode in supersonic boundary layer,” *Appl. Math. Mech.* **38**, 1109–1126 (2017).
- ³⁷A. Maslov, A. Shplyuk, A. Sidorenko, and D. Arnal, “Leading-edge receptivity of a hypersonic boundary layer on a flat plate,” *J. Fluid Mech.* **426**, 73–94 (2001).
- ³⁸K. D. Fong, X. Wang, and X. Zhong, “Numerical simulation of roughness effect on the stability of a hypersonic boundary layer,” *Comput. Fluids* **96**, 350–367 (2014).
- ³⁹R. Song, M. Dong, and L. Zhao, “Revisit of the oblique-breakdown regime in supersonic boundary layers and mechanism of the extra amplification of streak modes,” *Phys. Fluids* **34**, 104110 (2022).
- ⁴⁰F. M. White, *Viscous Fluid Flow* (McGraw-Hill, New York, 1991), Vol. 2.
- ⁴¹J. Sivasubramanian and H. F. Fasel, “Direct numerical simulation of transition in a sharp cone boundary layer at Mach 6: Fundamental breakdown,” *J. Fluid Mech.* **768**, 175–218 (2015).
- ⁴²C. Hader and H. F. Fasel, “Direct numerical simulations of hypersonic boundary-layer transition for a flared cone: Fundamental breakdown,” *J. Fluid Mech.* **869**, 341–384 (2019).
- ⁴³Z. Zhang and X. Wu, “Generation of sound waves by nonlinearly evolving ring-mode coherent structures on a turbulent subsonic circular jet: A comparative study of two mechanisms,” *Acta Mech. Sin.* **39**, 322272 (2023).
- ⁴⁴T. Herbert, “Secondary instability of boundary layers,” *Annu. Rev. Fluid Mech.* **20**, 487–526 (1988).
- ⁴⁵L. L. Ng and G. Erlebacher, “Secondary instabilities in compressible boundary layers,” *Phys. Fluids A: Fluid Dyn.* **4**, 710–726 (1992).